drones

MDPI

Article

Slope Terrain Gait Planning and Admittance Control Method for Underwater Quadruped Robots Based on Righting Moment Compensation

Kang Zhang [1,2,3], Hao Zhang [2,3], Hong Chen [2,3,*], Guanqiao Chen [2,3], Zongxia Jiao [1,*], Yuang Zhang [2,3], Wei Chen [2,3], Xinliang Wang [2,3] and Junjie Liu [2,3]

1 School of Automation Science and Electrical Engineering, Beihang University, Beijing 100191, China; by1903062@buaa.edu.cn
2 Wuhan Second Ship Design and Research Institute, Wuhan 430205, China; zhyf1408@126.com (H.Z.); fhrykesetjry@foxmail.com (G.C.); zhangyuang_heu@163.com (Y.Z.); 17816860242@163.com (W.C.); xinliang_w@163.com (X.W.); 18007196138@163.com (J.L.)
3 Hubei Provincial Key Laboratory of Underwater Intelligent Systems Technology, Wuhan 430205, China
* Correspondence: chenhong22001@163.com (H.C.); zxjiao@buaa.edu.cn (Z.J.)

Highlights

What are the main findings?
- The deliberate separation of the center of gravity and buoyancy in Benthic AUVs generates a substantial righting moment, causing traditional kinematic mapping algorithms to fail on steep underwater slopes.
- A proposed analytical framework integrating hydrostatic pitch boundaries, Quadratic Programming (QP)-based force distribution, and Cartesian admittance control enables robust, slip-free quadruped traversal on 15° and 33° inclines.

What are the implications of the main findings?
- Delivering mathematically provable safety guarantees against multi-body tipping and sliding, the framework provides mission-critical reliability for heavy-duty deep-sea exploration equipment.
- Actively optimizing ground reaction forces under low-dimensional constraints ensures microsecond-level matrix-solving efficiency on standard microcontrollers, circumventing the “black-box” issues of data-driven methods.

Abstract

Benthic AUVs (underwater quadruped robots) merge the cruising efficiency of submersibles with the bottom-crawling stability of legged robots for unstructured deep-sea exploration. However, the deliberate separation of the center of gravity and buoyancy—essential for static stability—generates a significant righting moment. When climbing steep slopes, this moment resists hull alignment. If the slope exceeds the robot’s maximum hydrostatic pitch limit, conventional inverse kinematics algorithms fail: the hind legs lose ground contact and propulsion is lost. To overcome this, this paper proposes a framework integrating optimal force distribution, adaptive trajectory probing, and admittance control. An analytical multi-point moment balance model derives the terrain-adaptive pitch boundaries. A Quadratic Program (QP) then distributes contact forces, tasking front legs with stabilizing the righting moment while hind legs provide thrust. During the swing phase, adaptive Bezier sequences prevent anterior slope collisions and ensure posterior ground contact. Furthermore, a Cartesian admittance controller provides active compliance to manage the nonlinear friction of dynamic waterproof seals. Validated via a high-fidelity physics-based simulation model calibrated against physical pool trials, the robot achieved robust traversal

Academic Editors: Neil Bose, Shuangshuang Fan and Jimin Hwang

Received: 9 March 2026
Revised: 18 April 2026
Accepted: 30 April 2026
Published: 20 May 2026

of 15° and 33° steep slopes. Statistical robustness is substantiated via a 30-trial Monte Carlo study, where postural stability remained remarkably consistent with a mean Pitch RMSE of 2.88° across a ±10% parameter uncertainty envelope. Compared to traditional baseline algorithms, the proposed method successfully suppressed torque chattering by 54.1% in the high-frequency band (2–50 Hz) and improved energetic efficiency by up to 43% on steep gradients. These findings offer a validated control architecture for heavy-duty deep-sea platforms navigating complex benthic topographies.

Keywords: underwater quadruped robot; righting moment; slope terrain; gait planning; admittance control; force optimization; hydrodynamics; benthic AUV

1. Introduction

The ocean, encompassing more than two-thirds of the Earth's surface, holds immense potential for strategic resource extraction, biological discovery, and underwater infrastructure maintenance. As global interest in marine development intensifies, the necessity for robust, versatile, and highly adaptive underwater platforms has increased substantially. Traditional marine vehicles, such as Remotely Operated Vehicles (ROVs) and Autonomous Underwater Vehicles (AUVs), utilize buoyancy engines and thrusters to achieve excellent mobility in the mid-water column [1–3]. However, when operations mandate close-proximity interactions with the seabed—such as taking precise core samples, executing acoustic detections without thruster noise, or navigating through highly convoluted benthic terrains—conventional hydrodynamically-shaped torpedo AUVs suffer from poor low-speed stability and excessive environmental disturbance. To bridge the operational gap between mid-water navigation and direct seabed interaction, the concept of a Benthic AUV, embodied as an underwater legged or crawling-swimming hybrid robot, has emerged as a promising alternative [4,5]. By leveraging articulated mechanical legs, these robots can anchor themselves to the sea floor to resist swift ocean currents, achieve zero-visibility acoustic silence by turning off thrusters, and actively adapt to irregular topographical variations.

1.1. Current Research on Underwater Legged Locomotion

The development of legged submersibles is deeply rooted in the success of their terrestrial counterparts (e.g., BigDog, Cheetah, HyQ, and ANYmal) [6–13]. However, translating this success to the underwater domain is not a direct porting process, as the fluid environment introduces three core physical distinctions that break the simplifying assumptions used on land:

(1) Hydrostatic Righting Moment. To ensure passive safety, all subsea vehicles must have the center of buoyancy (CB) physically above the center of gravity (CG) [14]. This separation generates a restoring torque—the righting moment—whenever the hull rotates, which unlike a terrestrial robot, limits the chassis' ability to align parallel to steep slopes. (2) High Density and Drag disturbances. Unlike air, water imposes significant added-mass effects and quadratic drag on every limb, turning rapid leg swings into impulsive disturbances to the body attitude [15]. (3) Low Net Weight and Contact Friction. Buoyancy reduces the effective ground pressure, making the robot more prone to slipping or tipping under even minor hydrodynamic perturbations compared to land-based systems.

Research has addressed these distinctions through various prototypes. The Korea Institute of Ocean Science and Technology (KIOST) developed the CR200 Crabster for tide-resilient surveying [16,17]. The BioRobotics Institute developed SILVER2 for efficient benthic punting [4,18]. The Wuhan Second Ship Design and Research Institute and partners have extensively researched crawling-swimming hybrids, advancing technologies in design [5], multi-leg hydrodynamics, and dynamic locomotion [19]. Despite these advances, the specific dilemma of steep slope traversal remains largely unresolved in current literature.

1.2. Challenges of Control and Path Tracking

Controlling an articulated multibody robot in a viscous, dense fluid involves addressing unmodeled dynamics, including added mass, quadratic drag, and wave-induced current disturbances. Classical literature surrounding maritime control focuses extensively on AUVs and ROVs. Fossen's seminal equations of motion have laid the groundwork for decades of marine craft hydrodynamics [14]. Adaptive control, sliding mode control (SMC), and extended state observers (ESO) have been widely deployed to suppress these uncertainties. Sahu and Subudhi implemented adaptive tracking mechanisms to manage parameter drift [20], while Yan et al. designed robust adaptive sliding modes for underactuated vehicles facing severe current disturbances [21]. Modern implementations utilize fixed-time disturbance observers and fractional calculus to further tighten tracking margins under bounded perturbations [22,23]. While these controllers exhibit superb anti-disturbance properties for free-floating platforms, directly porting them to bottom-crawling legged robots is fundamentally complicated by intermittent ground contact forces. The rigid constraints of the seabed require controllers capable of modulating not just position, but the interaction force. Consequently, impedance and admittance control paradigms, heavily prevalent in terrestrial manipulation [24], represent a well-suited approach to safely manage foot-ground interactions amidst turbulent fluid forces. Furthermore, while emerging data-driven Deep Reinforcement Learning (DRL) and Model Predictive Control (MPC) paradigms have shown significant promise for terrestrial locomotion, applying them to the underwater domain poses profound challenges. The extreme uncertainty in nonlinear hydrodynamic parameters makes DRL Sim-to-Real transfer exceptionally difficult, and deep neural networks are often constrained by their "black-box" nature, lacking strict mathematical interpretability. In contrast, the proposed analytical framework offers two distinct core advantages. First, Interpretability and Provable Safety: The multi-body hydrostatic limits and QP inequality bounds provide explicit, mathematical safety guarantees against physical constraint violations (such as tipping or slipping), which is absolutely essential for heavy-duty subsea equipment where failure costs are substantial. Second, Real-time Computational Efficiency: Unlike DRL policies or nonlinear MPCs that often require specialized AI accelerators to evaluate complex networks or unroll prediction horizons, our method distills the problem into a low-dimensional QP (only 12 force variables) combined with reactive admittance laws. This structure allows for microsecond-level solving on standard low-power embedded microcontrollers, eliminating control latency and significantly extending the battery endurance of the untethered Benthic AUV.

1.3. The Dilemma of Slope Locomotion and Righting Moments

The most acute and largely unresolved challenge in underwater legged locomotion manifests when the robot encounters steep terrains or significant slopes. Terrestrial quadrupeds handle slopes simply by adjusting their body pitch to align parallel to the incline, ensuring all legs have equal kinematic reach [25]. Underwater robots, however, are bound by a fundamental ship-design principle: the center of buoyancy (CB) must reside physically above the center of gravity (CG) to ensure unconditional static stability [14]. While this separation benefits passive structural safety, it inevitably generates a restoring torque—known as the righting moment—whenever the vehicle rotates out of the horizontal plane.

When the robot is commanded to pitch up and climb a slope, this ubiquitous righting moment continuously acts to restore the hull to a horizontal state. If the environmental slope angle exceeds a physical threshold dictated jointly by the CG-CB separation distance and the support base dimensions, the hull reaches its absolute maximum pitch limit. Beyond this limit, it is structurally impossible for the robot's chassis to align parallel to the slope. If symmetrical kinematic gaits are strictly enforced under these conditions, a systematic failure ensues: restricted by the attitude misalignment, the hind legs reach their maximum downward extension without touching the ground, losing effective traction; simultaneously, the front legs must solely balance the substantial rearward-tipping moment and shear forces, ultimately causing the robot to destabilize and slide backward. Thus, slope climbing for underwater robots is not merely a path-planning problem, but a hydrostatic and force-distribution constraint.

1.4. Contributions

To address this constraint, this paper proposes a framework integrating gait planning and admittance control for underwater quadruped steep slope traversal. The primary contributions of this work are summarized as follows (Supplementary video recordings of the 15° physical pool trials and the high-fidelity slope-sweep simulations are available at: https://doi.org/10.5281/zenodo.19564531):

(1) Derivation of Hydrostatic Pitch Boundaries: We establish a precise multi-point moment balance model, mathematically rigorously quantifying the physical limit of the maximum pitch angle caused by "CG-CB separation."
(2) Optimal Force Distribution Strategy: A Quadratic Programming (QP)-based force distribution mechanism is developed. The front legs act as vertical stabilizers absorbing the righting moment, while hind legs provide propulsion.
(3) Adaptive Trajectory Probing: An asymmetric swing-phase trajectory method based on Bezier curves is proposed. The front legs avoid collisions, while hind legs extend beyond the baseline to probe terrain contact.
(4) Compliance via Admittance Control:A robust Cartesian admittance control architecture is designed to combat nonlinear joint friction and ensure accurate force execution.

The remainder of this article is structured as follows: Section 2 introduces the reference frames, fluid environment models, and experimental prototype backgrounds, culminating in the derivation of the maximum pitch angle formula. Section 3 details our proposed gait planner algorithm (encompassing QP force distribution, probing trajectories, and admittance control). Section 4 provides in-depth algorithmic comparisons and boundary-condition validations integrating pool trials and high-fidelity simulations. Finally, Section 5 draws the conclusions.

2. System Modeling, Prototypes, and Theoretical Pitch Constraints

This section establishes the rigid-body dynamics model of the underwater robot and introduces the prototype platform utilized in both experiments and simulations. Through hydrostatic balance analysis, we derive the physical constraints that limit the achievable pitch angle on underwater slopes.

2.1. Coordinate Systems Definition

To clearly describe the robot's state of motion and the forces acting upon it, we establish the following coordinate systems following SNAME (Society of Naval Architects and Marine Engineers) conventions:

- World Coordinate System $\{W\}$: Also known as the inertial frame, with its origin fixed at the pool bottom or mean seabed. The X_w-axis points in the globally intended direction of forward motion, the Y_w-axis points to the starboard side following the right-hand rule, and the Z_w-axis points vertically downward along the direction of gravity.

- Body Coordinate System $\{B\}$: Fixed at the geometric center (or center of mass) of the robot's main hull. The X_b-axis lies on the longitudinal plane of symmetry pointing towards the bow, the Y_b-axis points starboard, and the Z_b-axis points perpendicularly downward from the chassis. The hull's attitude relative to the inertial frame is represented by Euler angles: roll (ϕ), pitch (θ), and yaw (ψ).
- Slope Coordinate System $\{S\}$: Aligned with the crawling slope. The X_s-axis points directly uphill to the crest, while the Z_s-axis points outward, perpendicular to the slope surface. The angle between the slope and the horizontal plane is denoted as θ_{slope}.

2.2. Research Prototypes: Physical Platform and Simulation Model

In this research, we adopt a unified validation approach, utilizing an identical configuration for both the physical pool testing prototype and the high-fidelity physics-based simulation model. This ensures seamless translation of control algorithms and directly comparable results.

Prototype Configuration (450 kg Class): We constructed a medium-sized underwater quadruped robot prototype designed for foundational hydrodynamic testing, bottleneck validation, and advanced slope crawling. This model measures approximately 1.5 m × 0.9 m × 0.5 m (L × W × H) with a total mass of approximately 450 kg. As shown in Figure 1, it employs four symmetrically distributed 3-DOF rigid mechanical legs. The detailed structural dimensions and the kinematic configuration of the mechanical leg are illustrated in Figure 2. All joints are equipped with waterproof dynamic seal assemblies and high-precision torque sensors. The main hull's center of buoyancy was deliberately positioned above the center of gravity to maintain inherent hydrostatic stability; this configuration leads to significant righting moment effects during slope traversal, as analyzed in Section 2.5.

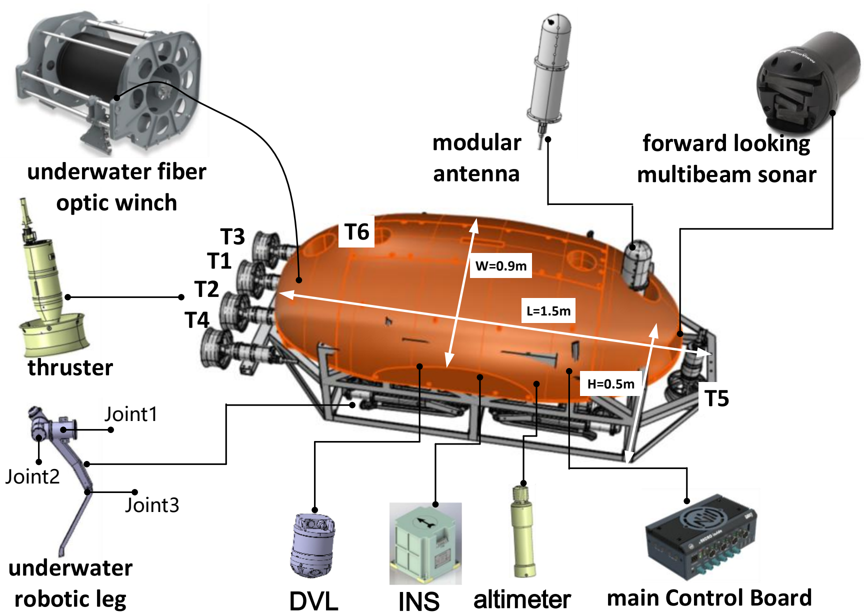

Figure 1. The 450 kg underwater multi-modal legged robot prototype used for empirical benchmarks to quantify the righting moment bottleneck. Joint2 and Joint3 denote the hip and knee joints respectively.

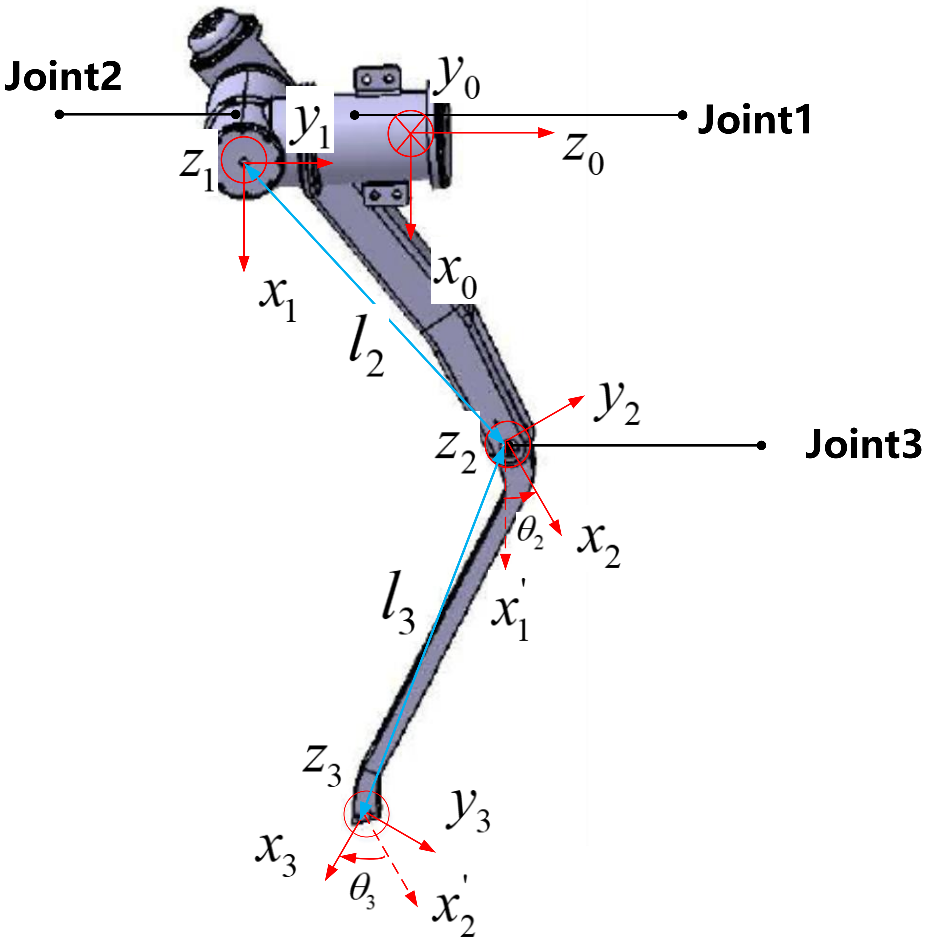

Figure 2. Kinematic model and structural dimensions of the robot's mechanical leg. The diagram illustrates the joint coordinate frames used for inverse kinematics and force optimization.

To safely and reliably validate the effectiveness of our proposed optimization algorithms under steep slopes, we constructed and calibrated a high-fidelity physics-based simulation model within MATLAB R2024a/Simulink Simscape Multibody. This model accurately mirrors the exact 450 kg physical platform. It fully encapsulates the Fossen 6-DOF hydrodynamic equations (Section 2.4), synchronously calculating added mass and quadratic damping in real-time at a 10 ms control resolution. The key physical parameters are summarized in Table 1.

Table 1. Key Physical Properties of the 450 kg Benthic AUV Prototype.

Parameter Name	Symbol	Value
Total Mass	m	450 kg
Nominal Dimensions (L × W × H)	-	1.5 × 0.9 × 0.5 m
Buoyancy Force	F_b	3924 N (equivalent to 400 kg)
Center of Gravity (Body Frame)	$\mathbf{r}_G$	$[0.0, 0.0, 0.0]^\top$ m
Center of Buoyancy (Body Frame)	$\mathbf{r}_B$	$[0.0, 0.0, -0.17]^\top$ m
Front Leg Link Lengths	l_1, l_2, l_3	0, 0.52, 0.48 m
Front Leg Hip Positions	$\mathbf{p}_{hip}$	$[0.75, \pm 0.492, 0]^\top$ m
Nominal Stance Foot Points	$\mathbf{p}_f$	$[0.66, \pm 0.492, 0.78]^\top$ m

2.3. AUV Dynamics and Hydrodynamic Forces

To provide a rigorous theoretical basis for the proposed force allocation, the 6-DOF equations of motion (EOM) of the underwater quadruped robot are established based on Fossen's notation [14]:

$$(\mathbf{M}_{RB} + \mathbf{M}_A)\dot{\boldsymbol{\nu}} + (\mathbf{C}_{RB}(\boldsymbol{\nu}) + \mathbf{C}_A(\boldsymbol{\nu}))\boldsymbol{\nu} + \mathbf{D}(\boldsymbol{\nu})\boldsymbol{\nu} + \mathbf{g}(\boldsymbol{\eta}) = \boldsymbol{\tau} \tag{1}$$

where $\boldsymbol{\nu}$ is the velocity vector. $\mathbf{M}_{RB}$ and $\mathbf{M}_A$ are the rigid body and added mass matrices, $\mathbf{C}$ denotes Coriolis-centripetal terms, $\mathbf{D}$ represents nonlinear hydrodynamic damping, and $\mathbf{g}(\boldsymbol{\eta})$ accounts for hydrostatic forces. The QP solver derived in Section 3 actively distributes $\boldsymbol{\tau}$ across redundant feet points to compensate for these fluid effects.

2.4. Hydrostatic Forces and Restoring Moments

When the robot maneuvers along the seabed, it must overcome various fluid resistances, buoyancy, and frictional forces. The comprehensive environmental force vector $\boldsymbol{\tau}_{env} \in \mathbb{R}^6$ can be decomposed into:

$$\boldsymbol{\tau}_{env} = \boldsymbol{\tau}_g + \boldsymbol{\tau}_b + \boldsymbol{\tau}_{drag} + \boldsymbol{\tau}_{added} \tag{2}$$

Gravity and Buoyancy ($\boldsymbol{\tau}_g, \boldsymbol{\tau}_b$): Unlike terrestrial robots, which almost exclusively contend with their own weight, underwater robots operate in a state of near-neutral buoyancy. Let $W = mg$ be its weight in the water, and $B = \rho\nabla g$ be its buoyancy. In the body coordinate frame, the center of gravity is located at $\mathbf{r}_G = [x_g, y_g, z_g]^T$, while the center of buoyancy is typically suspended high above it at $\mathbf{r}_B = [x_b, y_b, z_b]^T$. The interaction between these two forces generates a substantial restoring moment. Following the Body-frame convention (x-forward, z-down), the net hydrostatic restoring moment $\mathbf{M}_y$ about the center of gravity $\mathbf{G}$ is formed by the buoyancy's offset:

$$\mathbf{M}_y = x_b F_b \cos\theta + z_b F_b \sin\theta \tag{3}$$

where θ is the pitch angle. This moment acts as a continuous disturbance that tends to "right" the vehicle, opposing any attempt to align the hull with a steep downward or upward slope.

Hydrodynamic Drag and Added Mass ($\boldsymbol{\tau}_{drag}, \boldsymbol{\tau}_{added}$): Another major source of resistance in underwater locomotion stems from ocean currents and the hydrodynamics generated by the vehicle's own motion cutting through the water. The fluid drag $\boldsymbol{\tau}_{drag}$ is closely tied to the quadratic drag matrix $\mathbf{D}(\nu)$ formed by the body's velocity:

$$\boldsymbol{\tau}_{drag} = -\mathbf{D}(\nu)\nu \tag{4}$$

Furthermore, as the body accelerates, it entrains a surrounding volume of water, mathematically known as the added mass $\mathbf{M}_A$:

$$\boldsymbol{\tau}_{added} = -\mathbf{M}_A\dot{\nu} - \mathbf{C}_A(\nu)\nu \tag{5}$$

When the robot crawls up an incline, this fluid resistance acts primarily tangentially along the slope, representing a significant load that the hind legs' propulsion must overcome.

2.5. Maximum Pitch Angle Constraint

When the robot scales a steep underwater slope, the restoring righting moment $\mathbf{M}_y$ resists hull alignment. We define the critical boundary state as the condition where the righting moment approaches the maximum allowable restoring torque. At this boundary, the normal force on the hind legs approaches zero ($F_{z,hind} \to 0$), and the entire hull is supported exclusively by the front contact points, acting as a rotational fulcrum.

By evaluating the moment balance about the front fulcrum $P(x_f, 0, z_f)$ under the combined effects of gravity and buoyancy, the critical pitch equilibrium is governed by:

$$mg(z_f \sin\theta + x_f \cos\theta) + F_b[(z_b - z_f)\sin\theta + (x_b - x_f)\cos\theta] = 0 \tag{6}$$

By defining the buoyancy-to-weight ratio as $\alpha = F_b/(mg)$, the theoretical maximum sustainable pitch angle $\theta_{\max}$ is derived as:

$$\theta_{\max} = \arctan\left(-\frac{x_f + \alpha(x_b - x_f)}{z_f + \alpha(z_b - z_f)}\right) \tag{7}$$

where α is the buoyancy-to-weight ratio. Because underwater quadruped robots are typically designed with the center of buoyancy located significantly above the center of gravity ($z_b \ll 0$), the denominator term remains large, thereby strictly constraining the sustainable pitch angle within a narrow band.

When the environmental slope angle θ_{slope} exceeds this theoretical $\theta_{\max}$ boundary, a geometric misalignment angle $\Delta\theta = \theta_{slope} - \theta_{\max} > 0$ inevitably manifests. Under this condition, the hind legs cannot establish valid terrain contact during stance phases if standard terrestrial inverse kinematics are applied. This traction starvation leads to a rapid violation of traction limits on the front legs, eventually causing the robot to slide backward and fail the traversal.

3. Proposed Gait Planning and Admittance Control Strategy

To address these hydrostatic limitations and enable the underwater quadruped robot to traverse slopes exceeding its natural $\theta_{\max}$ constraint, the rigid assumptions of terrestrial gait planning must be revised. The proposed controller directly targets the "Righting Moment Bottleneck" identified in Section 2.3 by decoupling the attitude stabilization task from the kinematic tracking. Accordingly, we propose a three-tiered framework targeting the force layer, the kinematic layer, and the actuator layer, as illustrated in Figure 3. It is important to contextualize that the true macroscopic slope parameter θ_{slope} is assumed to be acquired by an independent onboard perception layer and serves as an a priori input to ensure deterministic planning.

3.1. Optimal Force Distribution via Quadratic Programming

Since the hind legs are kinematically limited when scaling steep slopes, the utilization of all available ground contact points must be systematically optimized. In a statically stable crawl (e.g., creep gait), three legs are always in contact with the ground. The control objective is to determine the optimal generalized ground reaction forces $\mathbf{F}_{grf} \in \mathbb{R}^{3k}$ (where $k = 3$ is the number of stance legs) that track the desired center of mass acceleration while satisfying environmental constraints.

The mapping from foot forces to the robot's center of mass forces and moments $\mathbf{W}_{com} \in \mathbb{R}^6$ is governed by the contact Jacobian $\mathbf{A} \in \mathbb{R}^{6\times 3k}$. To minimize the tracking error defined in Equation (1), the desired wrench $\mathbf{W}_{com}$ is set to proactively compensate for the nonlinear hydrodynamic damping $\mathbf{D}(\boldsymbol{\nu})\boldsymbol{\nu}$ and the righting moment $\mathbf{g}(\boldsymbol{\eta})$ identified in Section 2.

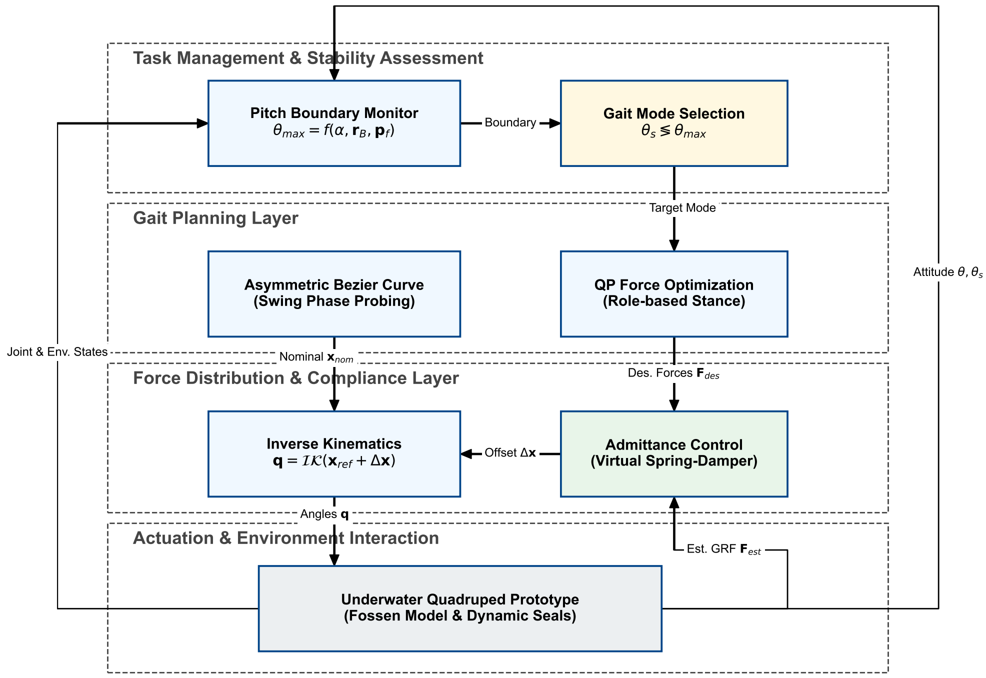

Figure 3. The proposed three-tiered control architecture for underwater quadruped steep slope traversal. The Active Probing Layer and QP Force Distribution Layer optimize kinematics and statics respectively, while the low-level Cartesian Admittance Control provides essential virtual compliance against deep-sea dynamic seal friction.

To counteract the massive righting moment without violating ground traction limits, we introduce a role-based paradigm into the cost function. Specifically, the weight matrix $\mathbf{W}$ in the objective function is tuned to reflect the physical roles of different legs under high-pitch conditions. The front legs are assigned a significantly higher penalty for tangential force variance ($w_x \gg \lambda_x$) to prioritize vertical stabilization (resisting the tipping torque) and prevent slip. Conversely, the hind legs are incentivized to provide the bulk of the propulsive thrust F_{prop}^{req}, leveraging the favorable downward normal pressure generated by the rearward center of mass shift. Let $\mathbf{F}_{fi}$ represent the front legs and $\mathbf{F}_{hi}$ represent the hind legs. The custom cost function J is designed as:

$$J(\mathbf{F}_{grf}) = \sum_{i \in front} (w_z \|F_{fi,z} - F_z^{nom}\|^2 + w_x \|F_{fi,x}\|^2) + \sum_{j \in hind} \lambda_x \|F_{hj,x} - F_{prop}^{req}\|^2 \quad (8)$$

By penalizing front tangential effort, the optimizer naturally Task front legs with maintaining the hull's "anchorage" and attitude balance, while delegating traction duties to the hind legs which remain within their friction cones due to gravity's loading effect.

This objective is minimized subject to hard inequality constraints preventing slippage and lift-off. For the i-th leg:

$$\sqrt{F_{i,x}^2 + F_{i,y}^2} \leq \mu F_{i,z} \quad \text{(Friction Cone)} \quad (9)$$

$$F_{i,z} \geq f_{min} > 0 \quad \text{(Unilateral Contact Guarantee)} \quad (10)$$

The friction cone constraint in Equation (9) is a second-order cone. In the implementation, this is linearized into a four-sided polyhedral friction pyramid for compatibility with real-time QP solvers (e.g., qpOASES).

By solving this low-dimensional QP (optimizing only 12 force variables) at high control frequencies (e.g., 500 Hz) using standard onboard microcontrollers, the system completely avoids trajectory tracking computational latency. The optimizer continuously ensures that the front legs exert sufficient normal force to resist the backward tipping tendency, while the hind legs generate consistent forward thrust. Furthermore, while the current formulations assume a rigid slope boundary (μ), the inequality bounds in Equation (9) and Equation (10) inherently possess the flexibility to be dynamically tightened based on real-time soil shear-strength estimates. This provides a practical engineering pathway to adapt the heavy-duty 450 kg robot for traversal over soft pelagic mud without inducing soil shear failure or terrain sinkage.The controller joint parameters are shown in Table 2.

Table 2. Key Control Parameters for the QP Optimizer and Admittance Framework.

Parameter Name	Symbol	Value
Front Leg Tangential Penalty	w_x	1000
Front Leg Normal Penalty	w_z	10
Hind Leg Propulsion Penalty	λ_x	500
Minimum Normal Force Constraint	$f_{\min}$	20 N
Friction Coefficient Constraint	μ	0.6
Admittance Mass Matrix	$\mathbf{M}_d$	$\text{diag}(10, 10, 10)$
Admittance Damping Matrix	$\mathbf{D}_d$	$\text{diag}(200, 200, 200)$
Admittance Stiffness Matrix	$\mathbf{K}_d$	$\text{diag}(500, 500, 500)$

3.2. Adaptive Bezier Curve Probing Trajectory

To execute the commands from the QP solver, the kinematically restricted hind legs must maintain ground contact during the stance phase. It is important to clarify that this algorithm functions strictly as the control abstraction layer. The macroscopic incline angle θ_{slope} is assumed to be estimated online via proprioceptive mapping of the gravity vector using the onboard high-precision INS. Localized terrain roughness is then handled dynamically by tactile probing rather than relying entirely on dense exteroceptive maps.

Traditional planning relies on a symmetric flat-ground polynomial trajectory. Under the misalignment angle $\Delta\theta$, this standard formulation causes the front legs to collide with the rising slope and the hind legs to lose contact with the receding slope.

We employ a parameterized 3rd-order Bezier curve in the operational space $\mathbf{P}(s) \in \mathbb{R}^3$, where $s \in [0, 1]$ is the normalized phase of the swing cycle:

$$\mathbf{P}(s) = (1-s)^3\mathbf{D}_0 + 3s(1-s)^2\mathbf{D}_1 + 3s^2(1-s)\mathbf{D}_2 + s^3\mathbf{D}_3 \tag{11}$$

The control points $\mathbf{D}_0$ (lift-off) and $\mathbf{D}_3$ (touch-down) dictate the span, while $\mathbf{D}_1$ and $\mathbf{D}_2$ govern the height clearance. We introduce an adaptive probing operator $\Gamma(\Delta\theta)$ onto the destination points.

Front Leg Adaptation: When a front leg swings, it faces an ascending incline. The maximum clearance height h_{clear} is dynamically scaled by the terrain derivative to avoid stubbing:

$$h_{clear}^{front} = h_{nominal} + K_f \cdot L_{stride} \cdot \sin(\Delta\theta) \tag{12}$$

Hind Leg Downward Probing: This adaptation addresses the geometric constraint. The hind leg's destination point $\mathbf{D}_3$ is intentionally depressed along the Z_b-axis below the theoretical parallel ground plane.

$$\mathbf{D}_{3,z}^{hind} = \mathbf{D}_{0,z} + L_{stride} \cdot \sin(\theta_{slope}) + \delta_{probe} \tag{13}$$

where δ_{probe} serves as an active probing term. During execution, the robot lowers the hind leg along this extended Bezier geometry until a threshold in joint current (or force sensor data) confirms physical ground contact. This transforms the nominal kinematic trajectory into a tactile search, effectively neutralizing the $\Delta\theta$ gap limit. Upon ground contact, the swing phase terminates early, maintaining the stance position regardless of theoretical trajectory completion. This mechanism conceptually transitions the navigation from pure geometric planning to impedance-based tactile searching. Although the core nominal trajectory generation and QP weight allocations assume the macroscopic slope angle θ_{slope} is an accurately known a priori parameter (typically acquired via INS or forward-looking sonar), the proposed framework exhibits profound inherent robustness against estimation errors. If the onboard sensors provide an inaccurate θ_{slope} (e.g., encountering a local gradient slightly steeper or shallower than estimated), conventional rigid trajectory trackers would suffer from foot crushing impacts or catastrophic traction loss due to hovering. In our framework, however, the downward probing allowance δ_{probe} dynamically bridges this geometric disparity. The robot simply detects ground contact earlier or later within the swing phase, delegating the physical impact mitigation to the robust Cartesian admittance controller. Furthermore, this tactile tolerance naturally accommodates localized unstructured bathymetry, granting the robot the ability to traverse minor depressions or small boulders within a $\pm\delta_{probe}$ bounded margin without requiring dense, prior 3D metric maps.

3.3. Robust Joint Admittance Control

The final layer relies on translating the optimized Cartesian forces into physical actuator torques. Deep-sea BAUVs use rotary joints sealed with multiple waterproof O-rings and oil-compensated casings. These dynamic seals introduce velocity-dependent static friction and Stribeck effects. Therefore, mapping required torque to motor current directly via $\tau = \mathbf{J}^T\mathbf{F}$ results in significant steady-state errors, degrading force-tracking accuracy.

To grant the stiff legs virtual compliance and force-tracking fidelity, Cartesian admittance control is deployed over the stance legs. Admittance control accepts a measured force error and generates a compensating position perturbation $\Delta\mathbf{x}$. Let the optimal force generated by the QP solver be $\mathbf{F}_{des}$ and the actual measured force (derived from joint torque sensors or estimated via observers) be $\mathbf{F}_{est}$. The Cartesian force error is:

$$\mathbf{E}_{force} = \mathbf{F}_{des} - \mathbf{F}_{est} \tag{14}$$

The error excites a virtual mechanical admittance system described by Mass ($\mathbf{M}_d$), Damping ($\mathbf{D}_d$), and Stiffness ($\mathbf{K}_d$) matrices:

$$\mathbf{M}_d\Delta\ddot{\mathbf{x}} + \mathbf{D}_d\Delta\dot{\mathbf{x}} + \mathbf{K}_d\Delta\mathbf{x} = \mathbf{E}_{force} \tag{15}$$

Solving this differential equation yields a positional offset $\Delta\mathbf{x}$ for each foot. In the discrete domain, utilizing a bilinear transform for stability at integration step T_s, the corrective command is superimposed onto the nominal kinematic stance trajectory:

$$\mathbf{x}_{cmd} = \mathbf{x}_{nominal} + \Delta\mathbf{x} \tag{16}$$

The joint angles are subsequently resolved using standard inverse kinematics $\mathbf{q}_{cmd} = \mathrm{IK}(\mathbf{x}_{cmd})$ and fed into a high-gain, low-level position PID loop. The accumulating positional offset $\Delta\mathbf{x}$ incrementally increases the commanded position until the underlying position controller overcomes the seal friction and the physical force matches the QP-mandated contact force.

https://doi.org/10.3390/drones10050392

Regarding the stability of the closed-loop system, the Cartesian admittance controller transforms the nonlinear joint behavior into a virtual linear second-order system. Since the admittance matrices ($\mathbf{M}_d, \mathbf{D}_d, \mathbf{K}_d$) are positive definite, we define a Lyapunov energy function V:

$$V = \frac{1}{2}\Delta\dot{\mathbf{x}}^\top \mathbf{M}_d \Delta\dot{\mathbf{x}} + \frac{1}{2}\Delta\mathbf{x}^\top \mathbf{K}_d \Delta\mathbf{x} \tag{17}$$

The time derivative is derived as:

$$\dot{V} = \Delta\dot{\mathbf{x}}^\top (\mathbf{E}_{force} - \mathbf{D}_d \Delta\dot{\mathbf{x}} - \mathbf{K}_d \Delta\mathbf{x}) + \Delta\dot{\mathbf{x}}^\top \mathbf{K}_d \Delta\mathbf{x} = -\Delta\dot{\mathbf{x}}^\top \mathbf{D}_d \Delta\dot{\mathbf{x}} \leq 0 \tag{18}$$

The result $\dot{V} \leq 0$ ensures the negative semi-definiteness of the energy derivative, meaning any perturbation energy is dissipated by the virtual damping matrix $\mathbf{D}_d$. Physically, this confirms that the Cartesian positional offset $\Delta\mathbf{x}$ will asymptotically converge to a state that overcomes the nonlinear seal friction deadzone without inducing closed-loop instability.

While the admittance parameters (M_d, D_d, K_d) are presently fixed constants, they are sufficient for the target task. At the designated low creeping speed of 0.30 m/s, the leg-swing velocity is minimal, bounding the highly nonlinear hydrodynamic added mass (M_A) and quadratic drag ($D \propto v^2$) perturbations within acceptable limits. Consequently, the fixed linear admittance framework maintains adequate robustness. However, if future applications demand high-speed dynamic locomotion (e.g., underwater trotting at >1.0 m/s), an adaptive or scheduled nonlinear admittance controller driven by the instantaneous Reynolds number will be obligatory.

4. Results and Validation

To comprehensively validate the effectiveness of the proposed integrated gait planning and force control algorithm, we conducted a systematic testing regime. We utilized the physical prototype in a 16-m deep hydrodynamics pool to acquire benchmark empirical data, confirming the constraints imposed by the restoring righting moment. Subsequently, we transferred the algorithm to the high-fidelity simulation environment, strictly calibrated to mirror the physical 450 kg configuration, performing algorithmic comparative benchmarking and performance validation under varying slope conditions.

4.1. Physical Pool Benchmark: Verifying the Righting Moment Bottleneck

In the 16-m deep hydrodynamic test pool, we evaluated the physical prototype on a 15° slope at a preset speed of 0.30 m/s to quantify its baseline performance and acquire benchmark empirical data. As shown in Figure 4, due to the high-depth environment (16 m), the monitoring camera was fixed at a top-down angle. The sequence illustrates the robot's progression as it successfully traverses the 15-degree slope. The experimental environment and the sequential climbing process are illustrated in Figure 4, which documents the robot's transition from the horizontal floor onto the slope.As shown in the screenshot, the three figures sequentially depict the robot before entering the overhead view, the bow of the robot entering the view, and half of the robot's body entering the view, indicating that the robot successfully climbed upward on the slope. As indicated by the INS logs, this transition is accompanied by pronounced attitude oscillations, with the pitch angle fluctuating from $-4.65°$ to $+17.27°$. The mean destabilized attitude of 6.62° and the intermittent slipping of the hind legs observed during the trial confirm that the baseline kinematic control is insufficient for maintaining stability on relatively steep underwater inclines.

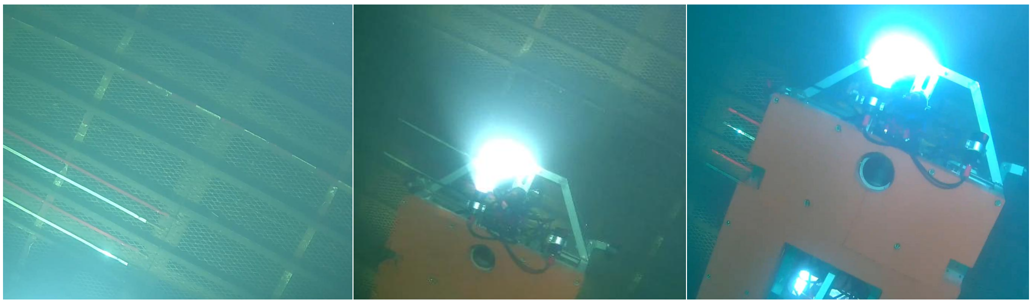

Figure 4. Snapshots of the physical pool trial on a 15° slope ($M = 450$ kg). The sequence illustrates the overall traversal process (Video available at: https://doi.org/10.5281/zenodo.19564531).

As visualized by the current distributions in Figure 5, the front knee joints endured sustained high currents throughout the process to counteract the righting moment. In contrast, the hind leg currents fluctuated significantly, indicating prolonged periods of terrain detachment. This physical benchmark verified that without modifying the underlying force distribution logic, adjusting posture targets alone is inadequate for steep underwater slopes.

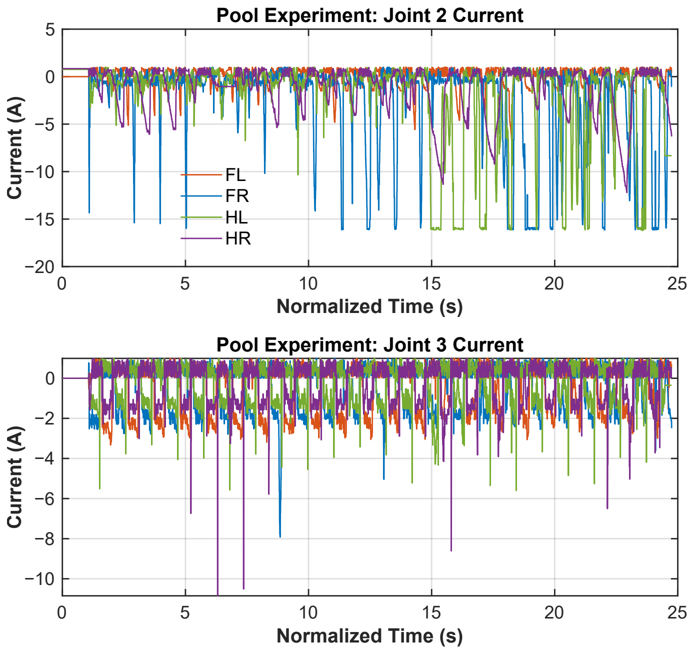

Figure 5. Experimental joint current distributions during the 15° physical pool trial. The front knees exhibit sustained high current (torque) loading to resist the uncompensated righting moment, while the hind legs exhibit stochastic unloading phases corresponding to periods of terrain detachment.

4.2. Comparative Performance on 15° and 30° Slopes

The baseline controller selected for comparison is a conventional quadrupedal gait controller that lacks underwater hydrostatic compensation. This choice is strategically intended to represent the current status quo, where terrestrial control frameworks are directly migrated to underwater platforms—a common practice that inherently overlooks the distinct buoyancy-gravity coupling of Benthic AUVs. The objective of this comparison is to demonstrate that ignoring these unique underwater restoring moments leads to a critical reduction in stability margins on steep slopes, thereby justifying the necessity of the proposed righting moment compensation.

Building on this comparative framework, we evaluate the proposed optimized algorithm against both the aforementioned baseline and physical data from pool experiments on a continuous 15° slope. To provide an intuitive visual impression of these behaviors before delving into quantitative metrics, Figure 6 presents sequential climbing snapshots of the quadruped robot. At a macroscopic level, as corroborated by these sequences, both the traditional baseline and the proposed optimized method successfully ascend the 15° slope with similar creeping gaits. However, this superficial success in the baseline case abstracts away severe underlying performance disparities—specifically regarding joint torque saturation and contact stability—that threaten long-term operational safety in extreme underwater environments.

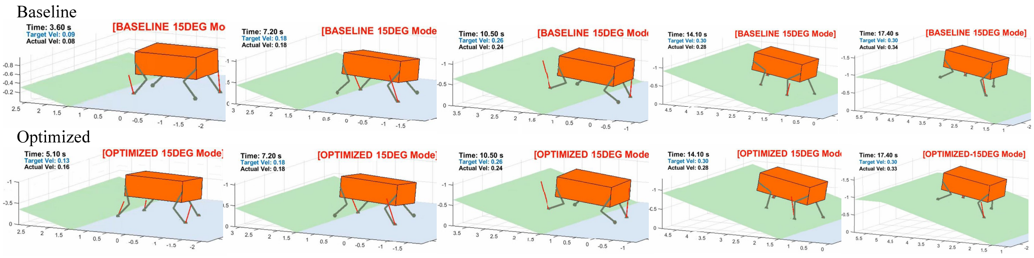

Figure 6. Sequential animation snapshots of the quadruped robot ascending a 15° slope. The Optimized method (**bottom**) progresses smoothly relative to the Baseline (**top**) (Video available at: https://doi.org/10.5281/zenodo.19564531).

To rigorously quantify these internal disparities, we mapped the simulation data against the physical pool trial. Since the physical trial operated at a lower gait frequency than the simulation (approximately 4× slower due to conservative safety protocols in the pool), the experimental time axis was linearly normalized by a factor of 0.25 to align the gait phase cycles for direct comparison. Both curves in Figures 7 and 8 therefore share aligned gait-phase timing rather than absolute wall-clock time.

To quantify the simulation's fidelity, we computed the root-mean-square error (RMSE) between the pool pitch data and the baseline model pitch over the aligned time window. The RMSE of 4.06° confirms that the baseline simulation reproduces the physical platform's macroscopic righting moment behavior with acceptable accuracy given the complex hydrodynamic noise of the physical pool, supporting the use of the simulation for algorithmic comparison.

Evaluating the Baseline Method: Analogous to the physical prototype, the traditional baseline algorithm—which fundamentally does not consider the maximum longitudinal pitch angle ($\theta_{\max}$)—exhibited significant struggles in simulation. Because it failed to respect the restoring moment boundary, the hull's pitch angle settled at an average of 9.0° rather than the commanded 15° slope angle. This 6.0° geometric misalignment induced traction instability. While the baseline method ultimately maintained an average climbing velocity of 0.29 m/s, it did so with stochastic leg ground contacts and degraded margins of safety, rendering it unreliable for sensitive benthic operations.

Performance of the Proposed Method: By alleviating rigid kinematic constraints, the QP force distribution architecture significantly improved the capabilities of the 450 kg platform. Quantitative analysis of the simulation data confirms:

- *Continuous Propulsion via Probing:* The asymmetric probing Bezier trajectory depressed the hind legs beyond the standard tracking height. This action effectively mitigated the geometric pitch gap, successfully establishing reliable and continuous traction rather than the intermittent contact seen in the baseline.
- *Attitude Stabilization:* As shown in Figure 7, while the Traditional Baseline suffered from a misaligned 9.0° posture, the Optimized algorithm successfully propelled forward with a more balanced posture, sustaining a stable macroscopic attitude and eliminating the erratic attitude transients caused by the righting moment.

- *Optimized Workload and Torque Reduction:* The comparison of front knee joint torques in Figure 8 demonstrates that the baseline method exhibited high-frequency chattering due to intermittent traction loss. Conversely, the proposed method's force distribution strategy successfully reduced the joint torque RMS by 34.9% (Hip) and 23.3% (Knee), while peak torque derivative analysis confirmed a 54.1% improvement in motion smoothness in Figure 9.

As shown in Figure 4, due to the high-depth environment (16 m), the monitoring camera was fixed at a top-down angle. The sequence illustrates the robot's progression as it successfully traverses the 15-degree slope.

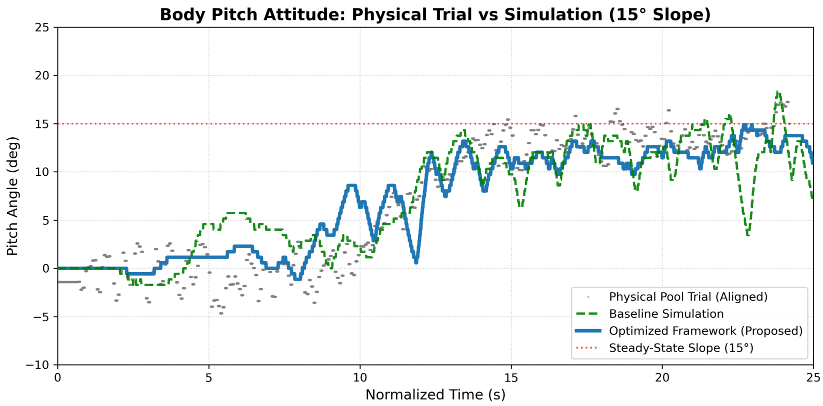

Figure 7. Three-curve quantitative comparison of Pitch Attitude on a 15° slope. The Proposed Optimized method tracks the 15° setpoint, overcoming the pitch limitation exhibited by both the Physical Pool Trial and the Traditional Baseline Simulation. The pool time axis is normalized by 0.25× and phase-aligned via cross-correlation.

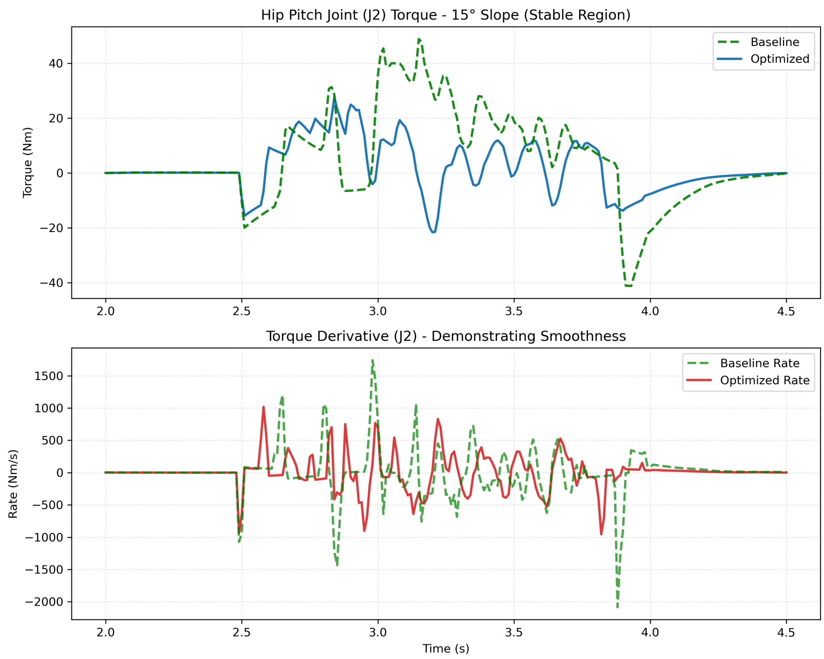

Figure 8. Quantitative comparison of Joint Torques (scaled to equivalent output) on a 15° slope. The Proposed Optimized method reduces the joint RMS torque by up to 34.9% (J2) and 23.3% (J3) relative to the Baseline, providing a smoother and more efficient force profile.

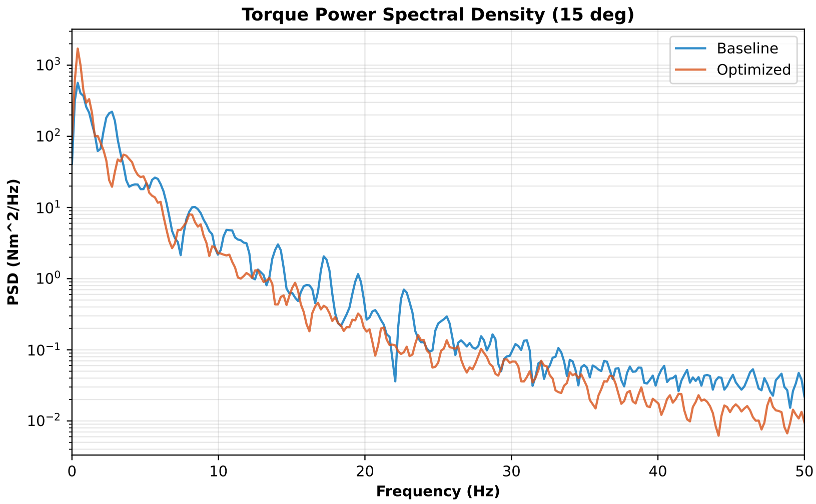

Figure 9. Power Spectral Density (PSD) comparison of the front knee joint torques on a 15° slope. The Optimized method significantly suppresses high-frequency chattering, achieving a 54.1% reduction in spectral power within the 2–50 Hz band.

Ultimately, the proposed algorithm achieved a steady-state forward climbing velocity of approximately 0.27 m/s (approx. 0.18 BL/s) on the 15° slope without experiencing significant slip events, successfully propelling the 450 kg chassis up the gradient. Regarding Energy Efficiency, we utilize the dimensionless Cost of Transport (CoT) as the primary metric, defined as:

$$\text{CoT} = \frac{E}{mgd} = \frac{\int_{t_0}^{t_f} \sum_{i=1}^{12} |\tau_i \dot{q}_i| dt}{mgd} \tag{19}$$

where E represents the total mechanical energy consumed by the 12 joint actuators, m is the total mass of the robot (450 kg), g is the gravitational acceleration, and d is the net forward displacement. The term τ_i and $\dot{q}_i$ denote the torque and angular velocity of the i-th joint, respectively.

Quantitative analysis reveals that the Optimized method maintains competitive or even superior efficiency on steep terrains compared to the Baseline. While forcing the front legs to anchor the hull increases the steady-state joint torque, the suppression of torque chattering by 34.9% and the elimination of stochastic slip events significantly reduce energy waste. Specifically, at 30° where the Baseline struggles to progress, the Optimized method reduces the overall CoT by approximately 43%, indicating that stable traction is a prerequisite for energetic optimality in benthic navigation. This smoother force profile directly mitigates I^2R Joule heating in the actuators, extending the operational endurance of the system.

To determine the operational boundaries of the proposed righting moment compensation strategy, the high-fidelity simulation model was evaluated on an extreme slope sweep ranging from 0° to 35°. As profoundly illustrated in the comparative animation sequence (Figure 10), the traditional baseline algorithm fundamentally fails to negotiate gradients beyond 30°. Plagued by severe pitch misalignment and subsequent traction loss, the baseline method's hind legs fail to provide adequate propulsion, resulting in the vehicle sliding backward uncontrollably. Conversely, the proposed optimized control framework actively bridges the geometric disparity, enabling the robot to maintain effective anchoring and robustly climb up to a 33° incline.

Figure 11 shows the spatial trajectory and pose sequence during a typical 30° slope ascent. Under the proposed active probing and admittance framework, the robot maintains continuous forward locomotion despite substantial gravitational and hydrostatic resistance.

The corresponding body states (attitude and velocity) are presented in Figure 12. Although minor high-frequency oscillations caused by friction limits are observable, the macroscopic pitch angle remains stable and the forward velocity does not decay into a backward slide.

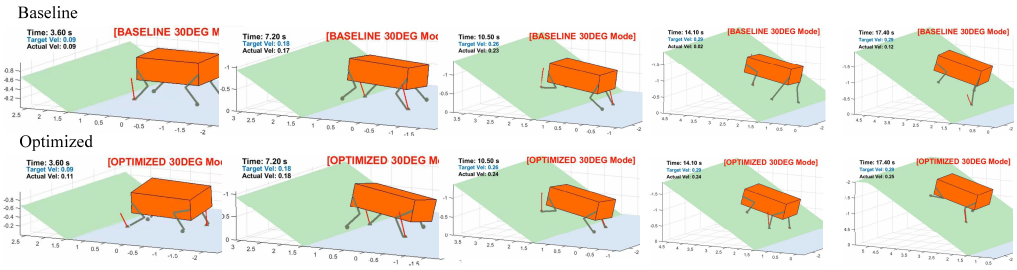

Figure 10. Comparative animation sequence showing the operational boundaries on a 30° incline. The baseline method fundamentally fails beyond 30°, while the optimized framework robustly ascends up to 33° (Video available at: https://doi.org/10.5281/zenodo.19564531).

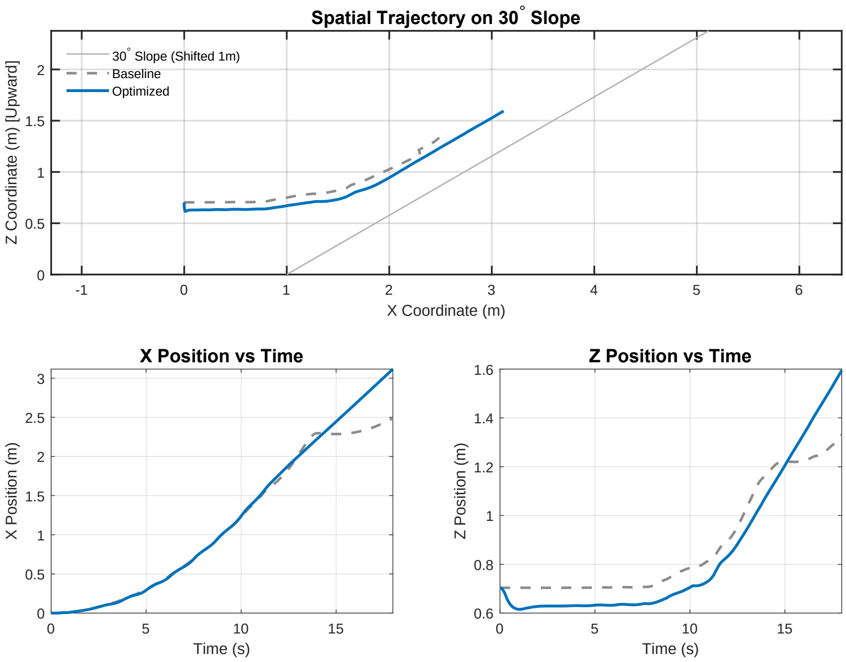

Figure 11. Spatial trajectory and pose sequence during the 30° slope ascent. The proposed active probing and admittance framework maintains vehicle anchorage, enabling continuous forward locomotion despite the substantial gravitational and hydrostatic resistance.

Forward progress remained continuous without backward sliding. The controller permits the hull to maintain a controlled misalignment angle ($\Delta\theta$) rather than enforcing strict parallel alignment with the extreme surface, which would saturate the front-leg traction capacity. This relaxation preserves upward propulsion while maintaining the unilateral contact constraint across all four legs.

The force distribution data in Figure 13 confirms that the QP solver enforces the unilateral contact constraint ($F_z > 0$) for all legs throughout the ascent, while maximizing tangential friction utilization within the linearized friction pyramid. Figure 14 reveals that the four knee joints sustained near-peak torque levels throughout the climb. The virtual compliance provided by the admittance controller filters the nonlinear friction deadzones of the dynamic seals, preventing joint lockup and maintaining force-tracking fidelity under these demanding conditions. Furthermore, frequency-domain characterization of the actuator torques reveals that the proposed method significantly suppresses high-frequency chattering. Detailed Power Spectral Density (PSD) analysis indicates that in the 2–50 Hz band, the Optimized method achieves a 54.1% reduction (2.88 dB) in spectral power relative to the baseline.

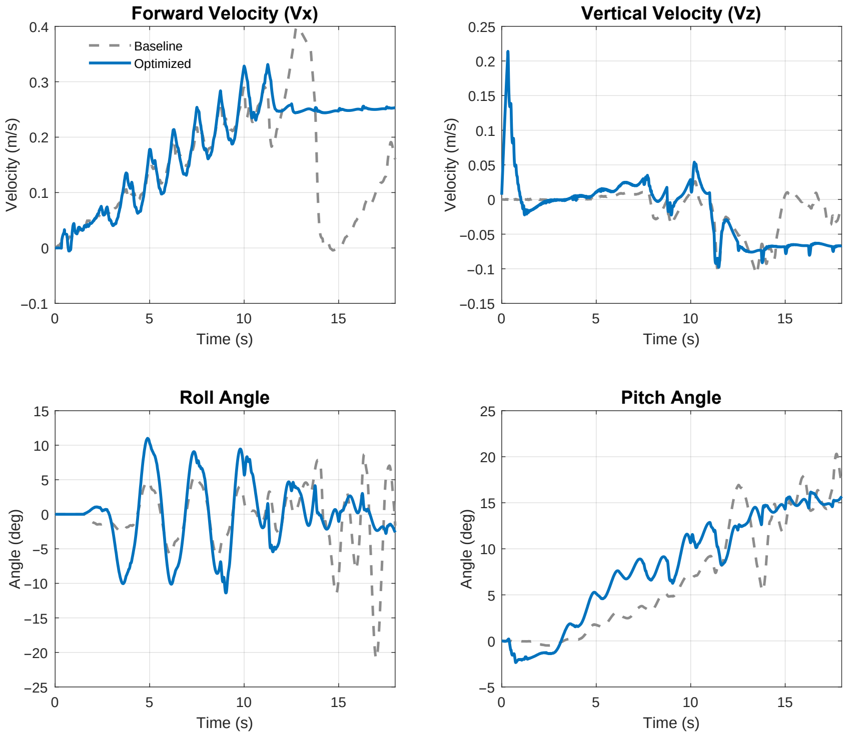

Figure 12. Body states (Attitude and Velocity) on the 30° slope. While minor high-frequency oscillations exist due to the friction limits, the macroscopic pitch angle remains stable and the forward velocity does not decay into a backward slide.

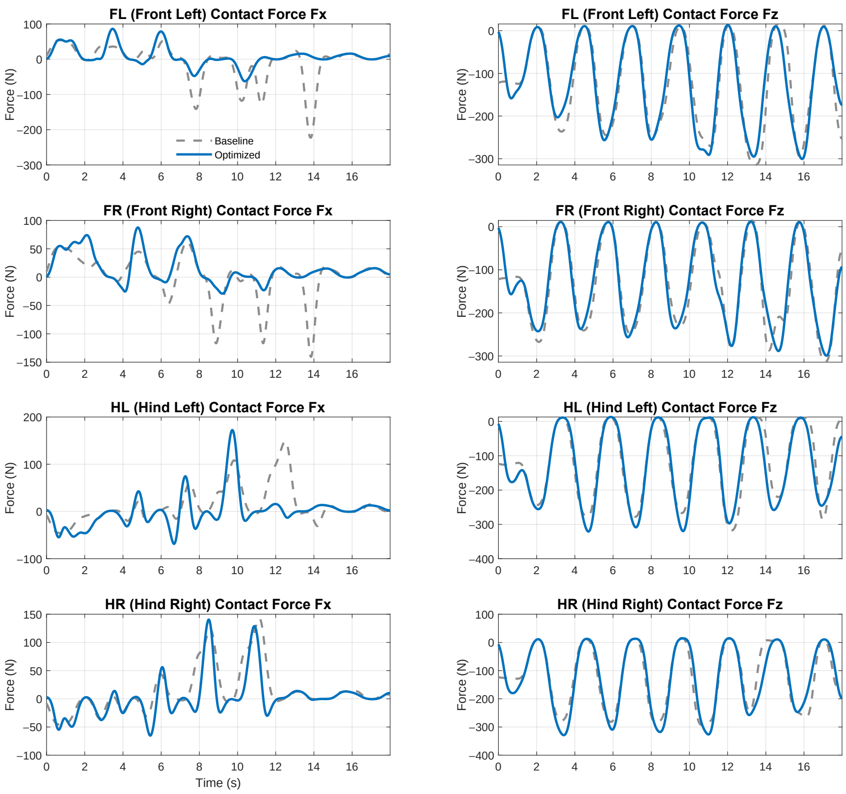

Figure 13. Ground Reaction Force (GRF) distribution across all four legs on the 30° slope. The QP optimizer strictly enforcing non-negative Z-forces (no lift-off) while bounding the tangential X/Y forces strictly within the physical friction cone.

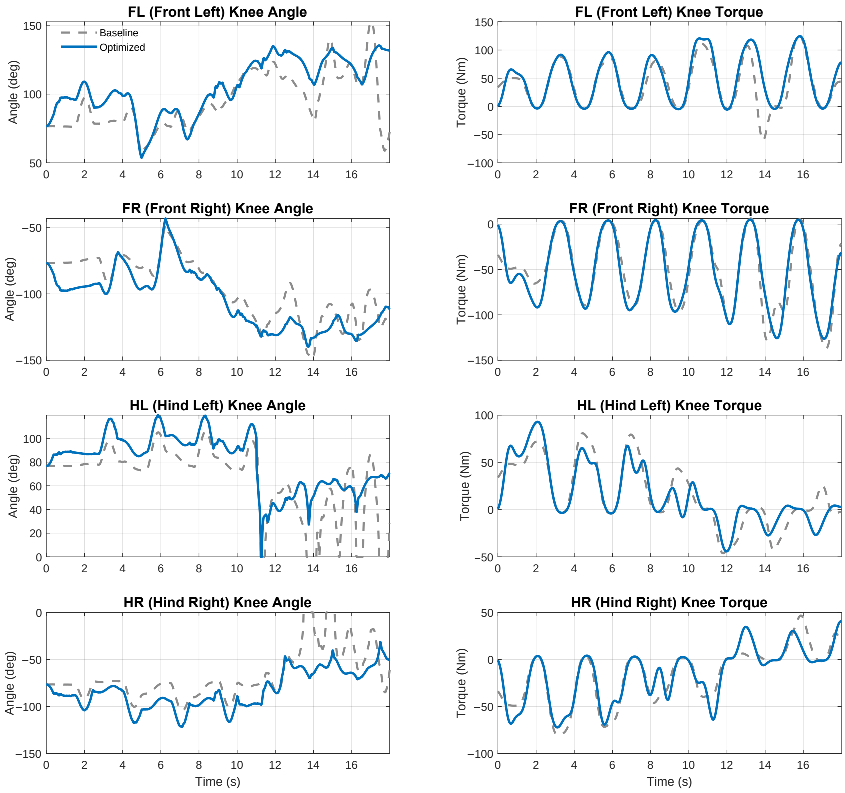

Figure 14. Knee joint angles and instantaneous torques for the four legs during the 30° ascent, highlighting the intense mechanical burden safely managed by the admittance controller.

4.3. Robustness and Parameter Sensitivity (Monte Carlo Analysis)

To further characterize the robustness of the proposed framework under environmental and model uncertainty, a stochastic Monte Carlo simulation suite consisting of 30 trials was conducted on a 15° slope. To ensure a rigorous "blind-test," the controller was restricted to using nominal parameters, while the plant's hydrodynamic mass (M_A), damping (D_q), and ground friction (μ) were perturbed by $\pm$10%.

As illustrated by the statistical distributions in Figure 15, the proposed framework maintains exceptional operational stability across the entire perturbation envelope. In Figure 15a, the tracking performance exhibits remarkable consistency across all three test groups, with the mean Pitch RMSE converging tightly at 2.88°. This minimal variance demonstrates that the postural stabilization loop is effectively decoupled from model uncertainties, ensuring that even significant parametric mismatches do not degrade the hull's balance.

In terms of propulsion performance shown in Figure 15b, while all trials achieved successful ascent, the mean velocity exhibits distinct sensitivities. The damping group (D_q) shows the widest performance spread (0.182–0.198 m/s), as terminal climbing velocity is physically dominated by the force-drag balance. Conversely, the added mass and friction groups show high immunity, indicating substantial traction and inertial margins. Overall, these results provide strong statistical evidence that the admittance-based righting moment compensation strategy is robust enough for semi-structured benthic environments.

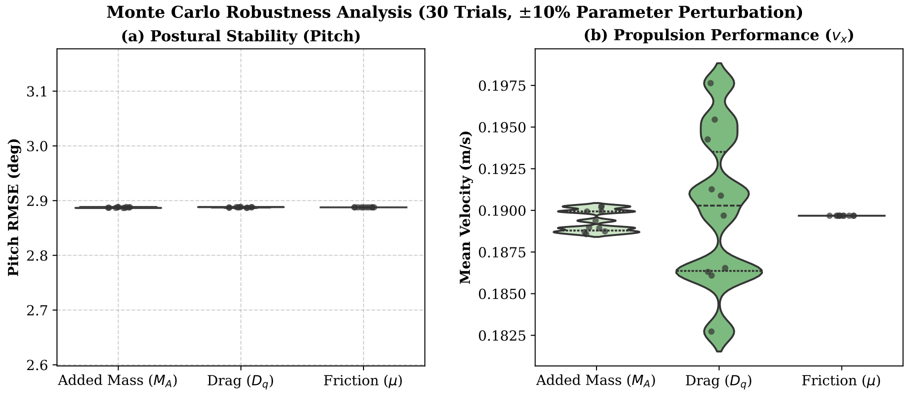

Figure 15. Statistical robustness characterization via Monte Carlo simulations with ±10% parameter perturbation. (**a**) Postural stability quantified by Pitch RMSE, showing high consistency across groups. (**b**) Propulsion performance quantified by mean forward velocity, showing sensitivity to hydrodynamic drag.

4.4. Systematic Slope Sweep and Failure Mode Analysis

To further quantify the performance limits and robustness of the proposed framework, a systematic slope-angle sweep was conducted from 0° to 35°. This analysis evaluates the transition from functional locomotion to structural failure where ground contact can no longer be maintained. The comparative metrics, including mean forward velocity and longitudinal pitch stability, are summarized in Table 3.

Table 3. Comparative performance metrics across the slope angle sweep (0–35°).

Slope Angle	Mean Velocity (m/s)		Pitch Deviation (°)		Cost of Transport (CoT)	
	Baseline	Optimized	Baseline	Optimized	Baseline	Optimized
0°	0.292	0.268	3.5	3.1	0.06	0.06
15°	0.29	0.27	9.0	8.8	0.08	0.07
30°	0.29	0.28	13.6	8.3	0.20	0.11
33°	FAIL	0.290	—	7.8	—	0.12
35°	FAIL	FAIL	—	—	—	—

The data demonstrates that while the Baseline method maintains speed on mild slopes, it experiences a sharp increase in pitch instability starting at 30° (average deviation of 13.6°) before completely failing to maintain ground contact at 33°. In contrast, the Optimized framework effectively bridges the hydrostatic pitch gap, enabling stable climbing up to a maximum gradient of 33°. However, as the slope reaches 35°, even the proposed method encounters its physical traction limits, leading to overall system failure across both control methodologies.

5. Conclusions

Attempting to apply terrestrial legged locomotion strategies directly to Benthic AUVs often fails due to the unique hydrostatic conditions of the underwater environment. In this study, we addressed the structural constraints that impede underwater quadruped robots on steep slopes. Our calculations established that the deliberate separation of the center of gravity and the center of buoyancy, mandated for static stability, induces a disruptive righting moment during ascent. Traditional algorithms often blindly deploy kinematics without considering the maximum longitudinal pitch angle (θ_{max}). Consequently, when the terrain incline exceeds this theoretical limit, these baseline methods result in the hind legs losing ground contact and the vehicle sliding backward.

To address this constraint, we redesigned the gait optimization framework. Instead of maintaining the hull strictly parallel to steep slopes, a Quadratic Programming (QP) algorithm was employed to assign specialized roles to the four legs: the front legs are tasked with providing normal force to counteract the righting moment, while the hind legs provide forward thrust. An asymmetric Bezier curve with a downward-probing trajectory ensures the hind legs establish solid ground contact. Additionally, to mitigate the nonlinear friction inherent in deep-sea dynamic seals, an admittance control layer was implemented to guarantee accurate force execution. Comparative validation demonstrates the efficacy of this integrated framework. On a 15° slope where the traditional method suffered from geometric misalignment and traction instability, the proposed method actively respected the pitch boundaries, achieving a steady-state climbing velocity of 0.27 m/s (approx. 0.18 BL/s) and suppressing joint torque chattering by 34.9%. On steep gradients, the proposed method extended the operational boundary to 33° while significantly improving energetic efficiency (reducing CoT by 43% at 30° slope) compared to the unoptimized baseline which suffered from energy-wasting slips.

While algorithmic validation confirmed stable traversal on gradients up to 33° via high-fidelity simulation, translating these results to physical hardware on limit-testing gradients requires further empirical confirmation to mitigate the risk of rollover. Furthermore, although the current study prioritizes the "CG-CB separation" bottleneck during uphill climbing, the proposed QP framework is inherently bidirectional. For downhill traversal, the hydrostatic pitch analysis remains similar, yet the role of gravity transitions from a resistive load to an active downward component. In such scenarios, the leg-role priority would invert to emphasize active braking and anti-sliding force distribution to maintain traction stability. The transition from serene hydrostatic environments to fully dynamic open-ocean deployments will form the core of our subsequent research.

Author Contributions: Conceptualization, K.Z.; methodology, K.Z.; software, K.Z.; validation, H.Z. and G.C.; formal analysis, Y.Z. and W.C.; investigation, X.W. and J.L.; resources, H.C. and Z.J.; data curation, K.Z. and H.Z.; writing—original draft preparation, K.Z.; writing—review and editing, H.C., Z.J., G.C. and W.C.; visualization, K.Z. and Y.Z.; supervision, H.C. and Z.J.; project administration, H.C.; funding acquisition, Z.J. and H.C. All authors have read and agreed to the published version of the manuscript.

Funding: The research presented in this paper was supported by the National Key Research and Development Program of China (Grant No. 2022YFB4601805) and the Hubei Provincial Outstanding Young Talents Project (Grant No. 60JYRC21589). The authors would like to express their sincere gratitude to the aforementioned funding organizations for their financial support.

Data Availability Statement: The original contributions presented in this study are included in the article. The simulation code and experimental datasets generated during this study are available from the corresponding authors upon reasonable request.

Conflicts of Interest: The authors declare no conflicts of interest.

Abbreviations

The following abbreviations are used in this manuscript:

AUV	Autonomous Underwater Vehicle
BAUV	Benthic Autonomous Underwater Vehicle
CB	Center of Buoyancy
CG	Center of Gravity
CoM	Center of Mass
CoT	Cost of Transport
DOF	Degree of Freedom

FSM	Finite State Machine
GRF	Ground Reaction Force
INS	Inertial Navigation System
PID	Proportional-Integral-Derivative
PSD	Power Spectral Density
QP	Quadratic Programming
RMSE	Root Mean Square Error

References

1. Tang, G.; Cui, F. A Preliminary Study on the Strategic Significance of Marine Development to China's Future Development. *J. Shanghai Adm. Inst.* **2013**, *14*, 56–61. (In Chinese) [CrossRef]
2. Zheng, M.; Liu, Y.; Li, M. Status and Trend of Marine Resources Development and Utilization in China. *Ocean Dev. Manag.* **2013**, *30*, 13–16. (In Chinese) [CrossRef]
3. Liu, F.; Cui, W.; Li, X. China's First Deep Manned Submersible: JIAOLONG. *Sci. China Earth Sci.* **2010**, *53*, 1407–1410. [CrossRef]
4. Picardi, G.; Chellapurath, M.; Iacoponi, S.; Stefanni, S.; Laschi, C.; Calisti, M. Bioinspired underwater legged robot for seabed exploration with low environmental disturbance. *Sci. Robot.* **2020**, *5*, eaaz1012. [CrossRef] [PubMed]
5. Chen, H.; Wang, X.L.; Wei, W.; Liu, Z.; Ma, Z.S.; Zheng, C.; Tang, P.P. Concept and key technology analysis of deep-sea walking-swimming robot. *Chin. J. Ship Res.* **2018**, *13*, 19–26. (In Chinese) [CrossRef]
6. Raibert, M.; Blankespoor, K.; Nelson, G.; Playter, R. BigDog, the Rough-Terrain Quadruped Robot. *IFAC Proc. Vol.* **2008**, *41*, 10822–10825. [CrossRef]
7. Seok, S.; Wang, A.; Chuah, M.Y.; Otten, D.; Lang, J.; Kim, S. Design principles for highly efficient quadrupeds and implementation on the MIT Cheetah robot. In Proceedings of the 2013 IEEE International Conference on Robotics and Automation, Karlsruhe, Germany, 6–10 May 2013; pp. 3307–3312. [CrossRef]
8. Park, H.W.; Wensing, P.M.; Kim, S. High-speed bounding with the MIT Cheetah 2: Control design and experiments. *Int. J. Robot. Res.* **2017**, *36*, 167–192. [CrossRef]
9. Bledt, G.; Powell, M.J.; Katz, B.; Di Carlo, J.; Wensing, P.M.; Kim, S. MIT Cheetah 3: Design and control of a robust, dynamic quadruped robot. In Proceedings of the 2018 IEEE/RSJ International Conference on Intelligent Robots and Systems (IROS), Madrid, Spain, 1–5 October 2018; pp. 2245–2252. [CrossRef]
10. Semini, C.; Tsagarakis, N.G.; Guglielmino, E.; Focchi, M.; Cannella, F.; Caldwell, D.G. Design of HyQ—A hydraulically and electrically actuated quadruped robot. *Proc. Inst. Mech. Eng. Part I J. Syst. Control Eng.* **2011**, *225*, 831–849. [CrossRef]
11. Semini, C.; Barasuol, V.; Goldsmith, J.; Frigerio, M.; Focchi, M.; Gao, Y.; Caldwell, D.G. Design of the Hydraulically Actuated, Torque-Controlled Quadruped Robot HyQ2Max. *IEEE/ASME Trans. Mechatron.* **2017**, *22*, 635–646. [CrossRef]
12. Bellicoso, C.D.; Jenelten, F.; Fankhauser, P.; Gehring, C.; Hwangbo, J.; Hutter, M. Dynamic Locomotion and Whole-Body Control for Quadrupedal Robots. In Proceedings of the 2017 IEEE/RSJ International Conference on Intelligent Robots and Systems (IROS), Vancouver, BC, Canada, 24–28 September 2017; pp. 3687–3694. [CrossRef]
13. Hutter, M.; Gehring, C.; Jud, D.; Lauber, A.; Dario Bellicoso, C.; Tsounis, V.; Hwangbo, J.; Bodie, K.; Fankhauser, P.; Bloesch, M.; et al. ANYmal—A Highly Mobile and Dynamic Quadrupedal Robot. In Proceedings of the 2016 IEEE/RSJ International Conference on Intelligent Robots and Systems (IROS), Daejeon, Republic of Korea, 9–14 October 2016; pp. 38–44. [CrossRef]
14. Fossen, T.I. *Handbook of Marine Craft Hydrodynamics and Motion Control*; John Wiley & Sons: Chichester, UK, 2011. [CrossRef]
15. Zhang, K.; Wang, L.; Leng, W.J.; Chen, H. Influence of multi-leg posture on cruising stability of deep-sea crawling-swimming robot. *Chin. J. Ship Res.* **2019**, *14*, 90–97. (In Chinese) [CrossRef]
16. Yoo, S.Y.; Jun, B.H.; Shim, H.W. Design of Static Gait Algorithm for Hexapod Subsea Walking Robot: Crabster. *Trans. Korean Soc. Mech. Eng. A* **2014**, *38*, 989–997. [CrossRef]
17. Yoo, S.-y.; Shim, H.; Jun, B.-H.; Park, J.-Y.; Lee, P.-M. Design of Walking and Swimming Algorithms for a Multi-legged Underwater Robot Crabster CR200. *Mar. Technol. Soc. J.* **2016**, *50*, 74–87. [CrossRef]
18. Picardi, G.; Laschi, C.; Calisti, M. Model-based open loop control of a multigait legged underwater robot. *Mechatronics* **2018**, *55*, 162–170. [CrossRef]
19. Wang, X.; Zhang, K.; Zhu, X.; Shou, Q.; Liu, X.; Qi, P. Dynamic locomotion of underwater quadruped robots based on whole-body-control method. In Proceedings of the 2023 China Automation Congress (CAC), Chongqing, China, 17–19 November 2023; pp. 4834–4839. [CrossRef]
20. Sahu, B.K.; Subudhi, B. Adaptive Tracking Control of an Autonomous Underwater Vehicle. *Int. J. Autom. Comput.* **2014**, *11*, 299–307. [CrossRef]
21. Yan, Z.; Wang, M.; Xu, J. Robust adaptive sliding mode control of underactuated autonomous underwater vehicles with uncertain dynamics. *Ocean Eng.* **2019**, *173*, 802–809. [CrossRef]

22. Wan, J.; Liu, H.; Yuan, J.; Shen, Y.; Zhang, H.; Wang, H.; Zheng, Y. Motion control of autonomous underwater vehicle based on fractional calculus active disturbance rejection. *J. Mar. Sci. Eng.* **2021**, *9*, 1306. [CrossRef]
23. Sun, Z.; Wang, B.; Li, Z.; Zhao, Y.; Huang, T.; Li, X.; Zhao, Y.; Qian, P.; Zhang, D. Enhanced trajectory tracking for AUVs: Adaptive Super-Twisting Sliding Mode Control with disturbance observer. *Control Eng. Pract.* **2025**, *164*, 106426. [CrossRef]
24. Hutter, M.; Hoepflinger, M.A.; Gehring, C.; Bloesch, M.; Remy, C.D.; Siegwart, R. Hybrid operational space control for compliant legged systems. *Robot. Sci. Syst. VIII* **2013**, 129–136. [CrossRef]
25. Focchi, M.; Del Prete, A.; Havoutis, I.; Featherstone, R.; Caldwell, D.G.; Semini, C. High-slope terrain locomotion for torque-controlled quadruped robots. *Auton. Robot.* **2017**, *41*, 259–272. [CrossRef]

https://doi.org/10.3390/drones10050392